



## **Runaway electron fluid model extension in JOREK and ITER relevant benchmarks**

Downloaded from: <https://research.chalmers.se>, 2024-08-27 16:25 UTC

Citation for the original published paper (version of record):

Bandaru, V., Hoelzl, M., Artola, F. et al (2024). Runaway electron fluid model extension in JOREK and ITER relevant benchmarks. *Physics of Plasmas*, 31(8). <http://dx.doi.org/10.1063/5.0213962>

N.B. When citing this work, cite the original published paper.

RESEARCH ARTICLE | AUGUST 02 2024

## Runaway electron fluid model extension in JOREK and ITER relevant benchmarks

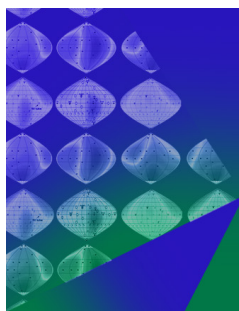
V. Bandaru ; M. Hoelzl  ; F. J. Artola ; O. Vallhagen ; M. Lehnen ; JOREK Team



*Phys. Plasmas* 31, 082503 (2024)

<https://doi.org/10.1063/5.0213962>






### Physics of Plasmas

### Features in Plasma Physics Webinars

Register Today!

 AIP  
Publishing

# Runaway electron fluid model extension in JOREK and ITER relevant benchmarks

Cite as: Phys. Plasmas **31**, 082503 (2024); doi: 10.1063/5.0213962

Submitted: 15 April 2024 · Accepted: 9 July 2024 ·

Published Online: 2 August 2024



View Online



Export Citation



CrossMark

V. Bandaru,<sup>1,2</sup> M. Hoelzl,<sup>2,a)</sup> F. J. Artola,<sup>3</sup> O. Vallhagen,<sup>4</sup> M. Lehnen,<sup>3,b)</sup> and JOREK Team<sup>c)</sup>

## AFFILIATIONS

<sup>1</sup>Indian Institute of Technology Guwahati, Assam 781039, India

<sup>2</sup>Max Planck Institute for Plasma Physics, 85748 Garching b. M., Germany

<sup>3</sup>ITER Organization, 13067 St. Paul Lez Durance, France

<sup>4</sup>Chalmers University of Technology, 412 96 Gothenburg, Sweden

<sup>a)</sup> Author to whom correspondence should be addressed: mhoelzl@ipp.mpg.de

<sup>b)</sup> Deceased before publication of the article.

<sup>c)</sup> See the author list of Hoelzl *et al.*, Nucl. Fusion **61**, 065001 (2021).

## ABSTRACT

We present details of recent extensions of the runaway electron (RE) fluid model implemented in the fusion magnetohydrodynamics code JOREK [M. Hoelzl *et al.*, Nucl. Fusion **61**, 065001 (2021)] to include the effects of partially ionized impurity species and deuterium neutrals. The model treats the interaction of runaway electrons with the background plasma via current-coupling. The code is separately benchmarked using ITER (<https://www.iter.org/>) relevant scenarios, with the GO [G. Papp *et al.*, Nucl. Fusion **53**, 123017 (2013)] code in relation to runaway electron beam formation and with the DINA [Khayrutdinov and Lukash, J. Comp. Phys. **109**(2), 193–201 (1993)] code in relation to simultaneous runaway beam formation and vertical plasma motion. Benchmark results show a decent agreement in both the cases, which are also discussed.

© 2024 Author(s). All article content, except where otherwise noted, is licensed under a Creative Commons Attribution (CC BY) license (<https://creativecommons.org/licenses/by/4.0/>). <https://doi.org/10.1063/5.0213962>

## I. INTRODUCTION

High energy relativistic runaway electron (RE) beams are expected to pose a major challenge for the upcoming fusion-grade tokamak experiments and possibly beyond (Hender *et al.*, 2007). Such runaway electron (RE) beams are formed in the aftermath of a thermal quench (TQ) of a plasma disruption, due to orders-of-magnitude rise in plasma electrical resistivity and parallel electric field resulting from the plasma cooling to relatively low temperatures (typically  $\sim 100$  eV or lower) during a thermal quench. The risk from REs being specific to relatively high plasma current future devices (e.g., ITER, <https://www.iter.org/>) arises due to the fact that RE beams form via RE seeds growing exponentially (the avalanche mechanism or secondary generation), with the number of e-foldings being proportional to the plasma current (Breizman *et al.*, 2019). Predictions for ITER till date indicate that it is very likely that nearly all the post-disruption plasma current (which would be a significant fraction of the pre-disruption current) would be carried by multi-MeV REs. An uncontrolled loss of such an RE beam would potentially lead to deep melting of the first-wall and possibly also damage the cooling pipes, which can, in turn, lead to large machine downtimes and repair costs. Possible solutions to the issue in the form

of avoidance or mitigation strategies have been proposed and have been evolving in recent years (Breizman *et al.*, 2019). Reliable assessment of the efficacy of such strategies warrant physical models that can describe the formation and transport of REs, as well as their co-evolution with the background plasma, its vertical displacement/motion toward the wall, and magnetohydrodynamic (MHD) instabilities.

Among the possible hierarchy of models, RE fluid models coupled to background plasma MHD (Matsuyama *et al.*, 2017; Bandaru *et al.*, 2019; Liu *et al.*, 2021; and Sainterme and Sovinec, 2024) tend to offer a reasonably comprehensive picture of the relevant physics, complementing higher-fidelity and relatively more expensive kinetic RE models. Such models have been used to study both standalone linear stability of the plasma in the presence of REs as well as complete non-linear evolution in experiments. In the present context of the massively parallel non-linear MHD code JOREK (Czarny and Huysmans, 2008; Hoelzl *et al.*, 2021), the RE fluid model first reported in Bandaru *et al.* (2019) has been subsequently used to simulate post-disruption RE beam termination dynamics in JET (Joint European Torus) (Bandaru *et al.*, 2021). In the current work, we present further extensions made to the RE fluid model in JOREK, specifically related to the inclusion of

the effects of impurities and deuterium neutral evolution during a disruption. Importance of these effects would be evident from the fact that massive material injection of impurities and/or deuterium (in one or more stages) forms the basis for some of the promising/mainstream strategies for RE mitigation in ITER. The extended model enables simulation of the full lifecycle of REs from their formation till termination and subsequent reformation, including the effects of multiple massive injections of material. We also present studies benchmarking the model in JOEUK with the GO code (Papp *et al.*, 2013) and the DINA code (Khayrutdinov and Lukash, 1993; Khayrutdinov *et al.*, 2001) with ITER relevant scenarios.

It has been shown in earlier works that the processes of radiative cooling, ionization/recombination associated with impurities, and deuterium neutrals can have a significant effect on the formation of RE beams (Vallhagen *et al.*, 2020). With regard to this aspect, our model in JOEUK is benchmarked with the one-dimensional predictions of the GO code. In addition, unlike thermal electrons, REs are not subjected to resistive decay and therefore RE beam formation can significantly alter the dynamics of plasma vertical motion [cold VDE (Vertical Displacement Event)] toward the wall. This is another important aspect as far as RE beam mitigation and electromagnetic wall loads are concerned. In this regard, JOEUK is benchmarked against the two-dimensional results of the DINA code for the co-evolution of the RE beam and cold vertical displacement event (cold VDE).

The paper is organized as follows. Section II describes the complete MHD plus RE fluid model in JOEUK, including impurities and deuterium neutrals. Benchmarking studies with GO and DINA are presented and discussed in Sec. III, followed by summary and outlook in Sec. IV.

## II. RUNAWAY ELECTRON FLUID MODEL EXTENSION IN JOEUK

The RE fluid model in JOEUK (Bandaru *et al.*, 2019; 2021) treats REs as a species separate from the background plasma. In the model, only the number density of REs ( $n_r$ ) is evolved that electromagnetically couples with the background plasma via current-coupling. The RE fluid model described earlier (Bandaru *et al.*, 2019; 2021) has been extended to include the effect of partially ionized impurities and deuterium neutrals. In addition to the independent effects of impurities and deuterium neutrals on the overall plasma dynamics, the computed RE sources become far more realistic as has been described in (Hesslow *et al.*, 2017; 2018; 2019). This is attributed to accounting for both the increased critical electric field as well as the number of electrons available for avalanche (bound electrons too contribute to the avalanche), with the latter effect dominating at high electric fields.

Using the reduced MHD approximation, the magnetic field  $\mathbf{B}$ , electric field  $\mathbf{E}$ , and the background plasma fluid velocity field are expressed, respectively, as  $\mathbf{B} = R^{-1}(\nabla\psi \times \hat{\mathbf{e}}_\phi) + (F_0/R)\hat{\mathbf{e}}_\phi$ ,  $\mathbf{E} = -F_0\nabla u - R^{-1}\partial_t\psi$ , and  $\mathbf{v} = -R\nabla u \times \hat{\mathbf{e}}_\phi$ , where  $R$  is the major radial coordinate,  $\psi$  is the poloidal magnetic flux,  $\hat{\mathbf{e}}_\phi$  is the unit vector in the toroidal direction, and  $F_0 u$  is the electric potential. The total mass density  $\rho$  that includes deuterium ions and impurities is defined as

$$\rho = \rho_i + \rho_{\text{imp}}, \quad (2.1)$$

where  $\rho_i$  is the deuterium/main ion density and  $\rho_{\text{imp}}$  is the impurity mass density that includes all charge states of the impurities. Individual charge states of the impurities are not evolved/tracked and instead a coronal equilibrium model is used to obtain the charge state

distribution as a function of temperature (Mosher, 1974). The background plasma fluid velocity is defined as  $\mathbf{u} = \rho^{-1}(n_i m_i \mathbf{u}_i + n_e m_e \mathbf{u}_e + n_{\text{imp}} m_{\text{imp}} \mathbf{u}_{\text{imp}})$  and is expressed as

$$\mathbf{v} = v_{\parallel} \hat{\mathbf{b}} - R(\nabla u \times \hat{\mathbf{e}}_\phi) - \frac{\nabla p_i \times \mathbf{B}}{n_i e B^2}, \quad (2.2)$$

where  $v_{\parallel}$  is the parallel component of the velocity, while the second and third terms represent the  $\mathbf{E} \times \mathbf{B}$  and diamagnetic drift velocities respectively. Both impurities as well as the deuterium ions are transported via advection with the above-mentioned fluid velocity and diffusion in the field parallel and perpendicular directions with respective diffusivities. Deuterium neutrals are only subjected to diffusive transport. All the species of the background plasma (deuterium ions, neutrals, and impurities) are assumed to be at the same temperature. Plasma thermal energy sinks include impurity radiation loss  $L_{\text{rad}}$  (line, Bremsstrahlung, and recombination radiation combined), Deuterium line radiation  $L_{\text{rad, Drays}}$ , and Deuterium continuous radiation  $L_{\text{rad, Dcont}}$ , while Ohmic heating due to thermal electrons serves as the heating source. More involved models for impurities and neutrals exist in JOEUK but are not considered here. These include an impurity fluid model without coronal equilibrium assumption (Hu *et al.*, 2021), a kinetic neutral model (Korving *et al.*, 2023), and a kinetic impurity model (Korving *et al.*, 2024).

The RE number density  $n_r$  is subjected to transport via the  $\mathbf{E} \times \mathbf{B}$  drift and parallel advection at the speed of light  $c$ . Often it is numerically challenging to advect REs at the speed of light, in which case the option of mimicking parallel transport instead by a large parallel diffusivity  $D_{\parallel, \text{RE}}$  exists (see Bandaru *et al.*, 2019 for a discussion on the same). The full governing equations in the normalized form for the background plasma and RE fluid would read as below [see Hoelzl *et al.* (2021) for details of normalization of variables in JOEUK]

$$\frac{1}{R^2} \frac{\partial \psi}{\partial t} = \frac{\eta}{R^2} \left( j - c \frac{F_0}{BR} n_r \right) - \frac{1}{R^2} [u, \psi] - \frac{F_0}{R^2} \frac{\partial u}{\partial \phi} + \frac{\tau_{\text{IC}}}{\rho} \left( \frac{1}{R} [p, \psi] + \frac{F_0}{R^2} \frac{\partial p}{\partial \phi} \right) - \frac{\eta_h}{R} \nabla^2 \left( \frac{j}{R} \right), \quad (2.3)$$

$$\nabla \cdot \left[ \rho R^2 \nabla_{\perp} \frac{\partial u}{\partial t} \right] = \frac{1}{2R} [R^2 |\nabla_{\perp} u|^2, R^2 \rho] + \frac{1}{R} [R^4 \rho \omega, u] - \frac{1}{R} [j, \psi] - \frac{F_0}{R^2} \frac{\partial j}{\partial \phi} - \frac{1}{R} [R^2, \rho T] + R \mu \nabla^2 \omega - \nabla \cdot [R^2 \nabla_{\text{pol}} u (\rho + \beta_{\text{imp}} \rho_{\text{imp}}) \times (\rho - \rho_{\text{imp}}) \langle \sigma v \rangle_{\text{rec, J}}], \quad (2.4)$$

$$j = \Delta^* \psi, \quad (2.5)$$

$$\omega = \nabla \cdot (\nabla_{\perp} u), \quad (2.6)$$

$$\begin{aligned} \frac{\partial \rho}{\partial t} = & R[\rho, u] + 2\rho \partial_z u - \left[ \frac{1}{R} [\rho v_{\parallel}, \psi] + \frac{F_0}{R^2} \partial_{\phi} (\rho v_{\parallel}) \right] + 2\tau_{\text{IC}} \partial_z p \\ & + \nabla \cdot [D_{\parallel, D} \nabla_{\parallel} (\rho - \rho_{\text{imp}}) + D_{\perp, D} \nabla_{\perp} (\rho - \rho_{\text{imp}})] \\ & + \nabla \cdot [D_{\parallel, \text{imp}} \nabla_{\parallel} \rho_{\text{imp}} + D_{\perp, \text{imp}} \nabla_{\perp} \rho_{\text{imp}}] \\ & + (\rho + \beta_{\text{imp}} \rho_{\text{imp}}) \rho_n \langle \sigma v \rangle_{\text{ion, J}}(T) - (\rho + \beta_{\text{imp}} \rho_{\text{imp}}) \\ & \times (\rho - \rho_{\text{imp}}) \langle \sigma v \rangle_{\text{rec, J}}(T) + S_D + S_{\text{imp}}, \end{aligned} \quad (2.7)$$

$$\begin{aligned}
\frac{\partial p}{\partial t} = & R[p, u] + 2\gamma p \frac{\partial u}{\partial Z} - v_{\parallel} \left[ \frac{1}{R} [p, \psi] + \frac{F_0}{R^2} \frac{\partial p}{\partial \phi} \right] \\
& - \gamma p \left[ \frac{1}{R} [v_{\parallel}, \psi] + \frac{F_0}{R^2} \frac{\partial v_{\parallel}}{\partial \phi} \right] + (\gamma - 1) \nabla \cdot [k_{\perp} \nabla_{\perp} T + k_{\parallel} \nabla_{\parallel} T] \\
& + (\gamma - 1) \frac{\eta}{R^2} \left( j - c \frac{F_0}{BR} n_r \right)^2 + \frac{\gamma - 1}{2} (v_{\parallel} B^2 + R^2 (\nabla_{\text{pol}} u)^2) \\
& \times (S_D + S_{\text{imp}}) + (\gamma - 1) \mu_{\parallel} [\nabla_{\text{pol}} (v_{\parallel} B)]^2 \\
& - (\rho + \beta_{\text{imp}} \rho_{\text{imp}}) \rho_{\text{imp}} L_{\text{rad}}(T_e) \\
& - (\rho + \beta_{\text{imp}} \rho_{\text{imp}}) (\rho - \rho_{\text{imp}}) L_{\text{rad, Dcont}} \\
& - (\rho + \beta_{\text{imp}} \rho_{\text{imp}}) \rho_n L_{\text{rad, Drays}}, \tag{2.8}
\end{aligned}$$

$$\begin{aligned}
\rho B^2 \frac{\partial (\rho v_{\parallel})}{\partial t} = & - \frac{\rho}{2R} [v_{\parallel}^2 B^2, \psi] - \frac{\rho F_0}{2R^2} \frac{\partial}{\partial \phi} (v_{\parallel}^2 B^2) + \frac{1}{R} [\psi, \rho T] \\
& - \frac{F_0}{r^2} \frac{\partial}{\partial \phi} (\rho T) + \mu_{\parallel} (T) B^2 \nabla^2 v_{\parallel}, \tag{2.9}
\end{aligned}$$

$$\begin{aligned}
\frac{\partial \rho_{\text{imp}}}{\partial t} = & R[\rho_{\text{imp}}, u] + 2\rho_{\text{imp}} \partial_Z u - \left[ \frac{1}{R} [\rho_{\text{imp}} v_{\parallel}, \psi] + \frac{F_0}{R^2} \partial_{\phi} (\rho_{\text{imp}} v_{\parallel}) \right] \\
& + \nabla \cdot (D_{\parallel, \text{imp}} \nabla_{\parallel} \rho_{\text{imp}} + D_{\perp, \text{imp}} \nabla_{\perp} \rho_{\text{imp}}) + S_{\text{imp}}, \tag{2.10}
\end{aligned}$$

$$\begin{aligned}
\frac{\partial \rho_n}{\partial t} = & \nabla \cdot (D_{\text{DN}} \nabla \rho_n) - (\rho + \beta_{\text{imp}} \rho_{\text{imp}}) \rho_n \langle \sigma v \rangle_{\text{ion, J}}(T) \\
& + (\rho + \beta_{\text{imp}} \rho_{\text{imp}}) (\rho - \rho_{\text{imp}}) \langle \sigma v \rangle_{\text{rec, J}}(T), \tag{2.11}
\end{aligned}$$

$$\begin{aligned}
\frac{\partial n_r}{\partial t} = & -f \frac{c}{F_0 R} \left[ R n_r, \psi \right] + F_0 \frac{\partial n_r}{\partial \phi} + (1 - f) \nabla \cdot (D_{\parallel, \text{RE}} \nabla_{\parallel} n_r) \\
& + R[n_r, u] + 2n_r \partial_Z u + S_{\text{Compton}} + S_{\text{Tritium}} + S_{\text{Avalanche}}. \tag{2.12}
\end{aligned}$$

The variables  $j$  and  $\omega$  represent the respective toroidal components of current density and vorticity, while  $p$  and  $\rho_n$  represent the total plasma pressure and Deuterium neutral mass density, respectively. Furthermore, the variables  $\tau_{\text{IC}}$  and  $\eta_h$  represent the respective normalized diamagnetic factor and hyperresistivity, while  $S_D$  and  $S_{\text{imp}}$  indicate external particle density sources for Deuterium ions and impurities. The variable  $D$  (with additional subscripts) represents the respective particle diffusivities, wherein the subscripts  $\parallel$  and  $\perp$  imply parallel and perpendicular components, while the subscripts  $D$ ,  $\text{imp}$ , and  $\text{DN}$  imply the species Deuterium ions, impurities, and Deuterium neutrals, respectively. The factor  $\beta_{\text{imp}}$  appearing in the above-mentioned equations is defined as  $\beta_{\text{imp}} = \frac{m_i}{m_{\text{imp}}} \langle Z_{\text{imp}} \rangle - 1$ , where  $\langle Z_{\text{imp}} \rangle$  is the average impurity charge. Furthermore, the terms  $\langle \sigma v \rangle_{\text{ion, J}}$  and  $\langle \sigma v \rangle_{\text{rec, J}}$  indicate the respective normalized velocity-averaged cross sections for ionization and recombination of Deuterium. Runaway volumetric sources include generation of RE seed via Compton scattering and tritium decay, along with the avalanche source. We now briefly describe the models used to compute the RE sources.

### A. RE seed and avalanche sources

As mentioned earlier, the effect of partially ionized impurities on the RE sources are included based on the work of [Hesslow et al., \(2017\)](#), (2018), and (2019). The implementation of the RE source

terms is briefly described hereby, wherein we also touch upon a few numerical aspects related to their computation. It must be noted that the implementation of sources including the effects of partially ionized impurities and deuterium neutrals ensures that JOREK uses state of the art RE generation terms now, which naturally leads to a much stronger RE beam formation than the previous code version would have given. The RE avalanche growth rate  $\Gamma = n_r^{-1} \frac{\partial n_r}{\partial t} = n_r^{-1} S_{\text{Avalanche}}$  is computed as

$$\Gamma = \frac{e}{m_e c \ln A_c} \frac{n_e^{\text{tot}}}{n_e} \frac{E_{\parallel} - E_c^{\text{eff}}}{\sqrt{4 + \bar{\nu}_s(p_*) \bar{\nu}_D(p_*)}}, \tag{2.13}$$

where  $n_e^{\text{tot}} = n_e + \sum_j n_j N_{ej}$  is the total electron density (free and bound electrons),  $n_e$  is the free-electron density,  $E_c^{\text{eff}}$  is the effective critical electric field,  $\bar{\nu}_s$  and  $\bar{\nu}_D$  are the normalized slowing down and deflection frequencies, respectively, and  $p_*$  is the effective critical momentum. The frequencies are normalized as  $\nu_s = \tau_c^{-1} \frac{\gamma^2}{p^3} \bar{\nu}_s$  and  $\nu_D = \tau_c^{-1} \frac{\gamma}{p^3} \bar{\nu}_D$  where  $p = \gamma v_{\parallel} / c$ ,  $\gamma = \sqrt{1 + p^2}$  and the relativistic collision time

$$\tau_c = \frac{4\pi \epsilon_0^2 m_e^2 c^3}{n_e e^4 \ln A_c} = \frac{m_e c}{e E_c} = \frac{1}{4\pi n_e c r_0^2 \ln A_c}. \tag{2.14}$$

Here,  $r_0$  is the classical electron radius and  $E_c = \frac{n_e e^3 \ln A_c}{4\pi \epsilon_0^2 m_e c^2}$  is the Connor–Hastie critical electric field. The relativistic electron–thermal electron Coulomb logarithm is given by  $\ln A_c = \ln A_0 + \frac{1}{2} \ln \frac{m_e c^2}{T} \approx 14.6 + 0.5 \ln (T_{\text{eV}} / n_{e20})$ , where the thermal electron–electron Coulomb logarithm  $\ln A_0 = 14.9 - 0.5 \ln n_{e20} + \ln T_{\text{KeV}}$ . There is no direct “formula” to evaluate the quantities  $E_c^{\text{eff}}$  and  $p_*$ , which are necessary to compute  $\Gamma$ . They have to be obtained iteratively by solving a non-linear equation each for  $E_c^{\text{eff}}$  and  $p_*$ .

The effective critical momentum  $p_*$  is evaluated using

$$p_* = \frac{\sqrt[4]{\bar{\nu}_s(p_*) \bar{\nu}_D(p_*)}}{\sqrt{E_{\parallel} / E_c}}, \tag{2.15}$$

with the slowing down and deflection frequencies given, respectively, by

$$\bar{\nu}_s = \frac{1}{\ln A_c} \left[ \ln A^{\text{ee}} + \sum_j \frac{n_j}{n_e} N_{ej} \left( \frac{1}{k} \ln(1 + h_j^k) - \beta^2 \right) \right], \tag{2.16}$$

$$\begin{aligned}
\bar{\nu}_D = & \frac{1}{\ln A_c} \left[ \ln A^{\text{ei}} + Z_{\text{eff}} \ln A^{\text{ei}} \right. \\
& \left. + \sum_j \frac{n_j}{n_e} \left( \frac{2}{3} (Z_j^2 - Z_{0,j}^2) \ln [(p \bar{a}_j)^{3/2} + 1] - \frac{2}{3} \frac{N_{ej}^2 (p \bar{a}_j)^{3/2}}{(p \bar{a}_j)^{3/2} + 1} \right) \right]. \tag{2.17}
\end{aligned}$$

In the above-mentioned equations, the electron–electron and electron–ion Coulomb logarithms are, respectively, given by  $\ln A^{\text{ee}} = \ln A_0 + \frac{1}{5} \ln \left[ 1 + \left( \frac{2(\gamma-1)}{P_{\text{Te}}^2} \right)^{2.5} \right]$  and  $\ln A^{\text{ei}} = \ln A_0 + \frac{1}{5} \ln \left[ 1 + \left( \frac{2p}{P_{\text{Te}}} \right)^5 \right]$ , where  $P_{\text{Te}} = \sqrt{\frac{2T}{m_e c^2}}$ . Furthermore,  $j$  refers to the impurity charge-state,  $Z_j$  is the charge number,  $Z_{0,j}$  is the ionization state,  $Z_{\text{eff}}$



$= \sum_j n_j Z_{0,j}^2 / n_e$  is the effective ion charge, and  $N_{e,j} = Z_j - Z_{0,j}$ . Likewise,  $\bar{a}_j$  is the effective ion size for charge state  $j$ ,  $h_j = \frac{p\sqrt{\gamma-1}}{I_j}$  with  $I_j$  being the mean excitation of the ion normalized to the electron rest energy,  $\beta = \frac{p^2}{1+p^2}$ , and  $k = 5$ .

The solution for  $p_*$  is obtained by solving Eq. (2.15) iteratively using the Newton–Raphson method starting with an initial guess. There also exist simplified approximate expressions for  $\bar{\nu}_s$  and  $\bar{\nu}_D$  that are valid in the high-energy or suprathermal RE limit and are, in principle, perfectly justified to be used as an alternative. However, during our benchmark studies, we found several instances where use of the approximate expressions led to issues with regard to the iterative solution for  $p_*$ . For instance, solutions found for  $p_*$  sometimes corresponded to a negative value of  $\nu_D$  and likewise we faced convergence issues at low values of  $p_*$ . On the other hand, the full expressions for  $\bar{\nu}_s$  and  $\bar{\nu}_D$  were observed to be numerically robust.

### 1. Evaluating $E_c^{\text{eff}}$

The effecting critical electric field can be evaluated by solving together the following two equations:

$$\frac{E_c^{\text{eff}}}{E_c} \approx \bar{\nu}_{s0} + \bar{\nu}_{s1} \left[ \left( 1 + \frac{\bar{\nu}_{D1}}{\bar{\nu}_{D0}} \right) \ln \frac{\bar{\nu}_{D0}}{2\bar{\nu}_{s1}} + \sqrt{2\delta + 1} \right], \quad (2.18)$$

$$\delta(E_c^{\text{eff}}) = \frac{\bar{\nu}_{D0}}{\bar{\nu}_{s1}^2} \left[ \frac{\bar{\nu}_{D0}\tau_{\text{syn}}^{-1}}{E_c^{\text{eff}}/E_c} + \phi_{\text{br}0} + \phi_{\text{br}1} \ln \left( \frac{\bar{\nu}_{D0}}{2\bar{\nu}_{s1}} \right) \right], \quad (2.19)$$

where  $\phi_{\text{br}0} = 0.35 \frac{\alpha}{\ln A_c} \sum_j \frac{n_j}{n_e} Z_j^2$ ,  $\phi_{\text{br}1} = 0.2 \frac{\alpha}{\ln A_c} \sum_j \frac{n_j}{n_e} Z_j^2$ ,  $\alpha \approx \frac{1}{137}$ , and  $\tau_{\text{syn}}$  is the synchrotron radiation-damping timescale normalized to  $\tau_c$  given by  $\tau_{\text{syn}}^{-1} = \frac{\tau_c \epsilon^4 B^2}{6\pi\epsilon_0 m_e^2 c^3} \approx \frac{1}{15.44 \ln A_c} \frac{B^2}{n_{c20}}$ . In addition, the constituents of the slowing down and deflection frequencies are given by

$$\begin{aligned} \bar{\nu}_{s0} &= 1 + \frac{1}{\ln A_c} \sum_j \frac{n_j}{n_e} N_{e,j} (\ln I_j^{-1} - 1), \\ \bar{\nu}_{s1} &= \frac{1}{2} \frac{1}{\ln A_c} \left( 1 + \sum_j 3 \frac{n_j}{n_e} N_{e,j} \right), \\ \bar{\nu}_{D0} &= 1 + Z_{\text{eff}} + \frac{1}{\ln A_c} \sum_j \frac{n_j}{n_e} \left( (Z_j^2 - Z_{0,j}^2) \ln \bar{a}_j - \frac{2}{3} N_{e,j}^2 \right), \\ \bar{\nu}_{D1} &= \frac{1}{\ln A_c} \sum_j \frac{n_j}{n_e} Z_j^2. \end{aligned}$$

Equations (2.18) and (2.19) can be combined (by eliminating  $\delta$ ) into a single cubic polynomial equation of the following form:  $ax^3 + bx^2 + cx + d = 0$  for the unknown variable  $x = E_c^{\text{eff}}/E_c$ . When the discriminant of the cubic equation is non-negative, an analytical solution for the real root  $x$  can be obtained without the need for an iterative scheme. In the case of a negative discriminant, we obtain an iterative solution for  $x$  using the Newton–Raphson scheme. It must be noted that the Newton–Raphson scheme, both for the computation of  $p_*$  as well as  $E_c^{\text{eff}}$ , does not guarantee a convergent solution for any initial guess, which necessitates the use of a new initial guess whenever the previous guess fails to produce a convergence of the iterations. An array of such initial guesses, covering a wide range, have been observed to work robustly in all the simulations performed so far with the model.

The runaway seed sources via Tritium decay and Compton scattering are modeled along the lines of [Martín-Solis et al. \(2017\)](#). There is currently no Dreicer source included in the RE fluid model. The RE seed generation rate via Tritium decay is computed as a fraction  $f$  of the rate of production of beta electrons and is given by

$$\left( \frac{\partial n_{\text{RE}}}{\partial t} \right)^{\text{Tritium}} = \lambda_T n_T = \ln 2 \left( \frac{n_T}{\tau_T} \right) f(W_{\text{crit}}),$$

where  $n_T$  is the tritium number density,  $\tau_T \approx 4500$  days is the half-life of tritium, and  $W_{\text{crit}} = m_e c^2 (\sqrt{p_*^2 + 1} - 1)$  is the critical runaway energy. The fraction  $f$  is given by ([Fülöp et al., 2020](#))

$$f(W_{\text{crit}}) \approx 1 - (35/8)w^{3/2} + (21/4)w^{5/2} - (15/8)w^{7/2},$$

where  $w = W_{\text{crit}}/Q$  and  $Q = 18.6$  keV.

The  $\gamma$ -rays/photons emitted by the activated plasma-facing components can cause Compton scattering of electrons into the runaway region of the momentum space. Note that all the electrons, bound and free, are available for Compton scattering because the energy of the gamma ray photons in ITER ( $\sim 0.1 - 10$  MeV) are much larger than the electron binding energies for Ar and Ne. In this case, the runaway generation rate can be evaluated as

$$\left( \frac{\partial n_{\text{RE}}}{\partial t} \right)^\gamma = n_e^{\text{tot}} \int \Gamma_\gamma(E_\gamma) \sigma(E_\gamma) dE_\gamma$$

with  $E_\gamma$  being the photon energy, the gamma flux energy spectrum  $\Gamma$  is approximated by

$$\begin{aligned} \Gamma_\gamma(E_\gamma) &\propto \exp(-\exp(-z) - z + 1) \\ z &= [\ln(E_\gamma [\text{MeV}]) + 1.2]/0.8, \end{aligned}$$

and the total compton cross section  $\sigma$  is given by

$$\begin{aligned} \sigma(E_\gamma) &= \frac{3\sigma_T}{8} \left[ \frac{x^2 - 2x - 2}{x^3} \ln \frac{1 + 2x}{1 + x(1 - \cos \theta_c)} \right. \\ &\quad + \frac{1}{2x} \left( \frac{1}{[1 + x(1 - \cos \theta_c)]^2} - \frac{1}{(1 + 2x)^2} \right) \\ &\quad \left. - \frac{1}{x^3} \left( 1 - x - \frac{1 + 2x}{1 + x(1 - \cos \theta_c)} - x \cos \theta_c \right) \right], \end{aligned}$$

where the Thomson scattering cross section  $\sigma_T = \frac{8\pi}{3} r_0^2$ ,  $x = E_\gamma/(m_e c^2)$  and the critical deflection angle  $\theta_c$  is given by  $\cos \theta_c = 1 - \frac{m_e c^2}{E_\gamma} \frac{W_{\text{crit}}/E_\gamma}{1 - (W_{\text{crit}}/E_\gamma)}$ .

It must be emphasized that the part of the compton RE source from live-activation by neutrons is typically far more dominant as compared to that of the compton RE source from large timescale decay ([Martín-Solis et al., 2017](#)), and therefore, the source is strongly dependant on the instantaneous fusion power. In addition, the fraction of pre-existing compton seed that survives the stochastic losses after TQ is unknown as far as purely post-TQ simulations are considered. Precise computation of compton seed would need one to consider pre-TQ generation as well as the complete dynamics of TQ and additionally reduce the source by several orders of magnitude after the TQ when practically very few fusion reactions occur. In this regard, computing the compton seed at burning rate even during the CQ (in this

as well as in previous studies) should be strictly viewed as a conservative or worst-case approach taken for the lack of high fidelity TQ simulations. Finally, while the governing equations in JOREK are, in general, solved using fully implicit numerics, all the RE source terms described above are treated explicitly.

### III. BENCHMARK WITH THE 1D CODE GO

#### A. Simulation setup

GO is a one-dimensional time-dependant code that couples RE-fluid with background plasma electrodynamics. The code has been in routine use for several years now among the RE research community in Europe. The present benchmark is based on some of the GO simulations presented in the work of Vallhagen *et al.* (2020) related to predictions for runaway electron (RE) formation in ITER in the presence of massive material injection, using state-of-the-art runaway electron sources that incorporate the effect of partially ionized impurities.

A circular DT-plasma with ITER-like dimensions is considered with major radius  $R = 6$  m, minor radius  $a = 2$  m, plasma current  $I_p = 15$  MA, and a uniform density of  $n_e = 10^{20} \text{ m}^{-3}$ . The plasma is assumed to consist of equal quantities of Deuterium and Tritium. At the initial state, the current density is given by a standard screw-pinch profile  $J = 1.69[1 - (r/a)^2]^{0.41} \text{ MA m}^{-2}$  and the temperature profile is given by  $T_e = 20[1 - (r/a)^2] \text{ keV}$ . At time  $t = 0$ , a certain mixture of Deuterium and Neon is assumed to appear within the plasma domain with a spatially uniform-density. This is intended to mimic an idealized massive material injection in the context of a disruption mitigation system in ITER. GO considers all species (electrons, main ions, and impurities) to be at the same temperature at all times. After the injection, the plasma is cooled down to very low temperatures. However, such a cooling of the plasma is executed in two phases. In the first phase, which lasts for a duration of 6 ms, the plasma is artificially cooled by forcing the temperature profile to drop exponentially according to

$$T(r, t) = T_f(r) + [T_0(r) - T_f(r)]e^{-t/t_0}$$

with  $t_0 = 1$  ms and  $T_f(r) = 50$  eV (uniform). With such a cooling, the plasma core temperature drops to  $T_e \approx 100$  eV. At this stage, artificial cooling is switched off and instead the plasma thermal energy is henceforth allowed to evolve. The thermal sources/losses include radiation (line, Bremsstrahlung, and recombination radiation), Ohmic heating, ionization-energy losses, and minor-radial heat diffusion with a diffusivity  $\kappa_{\perp} = 0.4 \text{ m}^2 \text{ s}^{-1}$  (equivalent to  $k_{\perp} = 4 \times 10^{19} \text{ m}^{-1} \text{ s}^{-1}$ ). During this phase, the plasma further cools down significantly (due mainly to radiation) from a core temperature of  $\approx 100$  eV to a few electron-volts. Due to much higher plasma resistivity at low temperatures, this increases the toroidal electric field significantly, leading to the conversion of thermal plasma current to RE current. Primary RE generation sources of Compton scattering and tritium decay are considered along with the RE avalanche source, while hot-tail source is not taken into

account. It has been shown in Vallhagen *et al.* (2020) that Dreicer seed was negligible, a result that substantiates a similar observation from the 1D simulations of Martín-Solis *et al.* (2017). It must be noted that since GO is one-dimensional, plasma equilibrium or dynamics is not taken into consideration in the simulations.

While the work of Vallhagen *et al.* (2020) considered Deuterium and Neon injection quantities scanned over a wide range of densities, for the purpose of the present benchmark we consider the two injection scenarios shown in Table I. Furthermore, it must be emphasized that the GO simulations corresponding to the above-mentioned cases in Vallhagen *et al.* have been rerun with a few changes in order to ensure the same conditions between JOREK and GO. These include using a coronal equilibrium model for impurities, fixed boundary condition for temperature, conducting wall at plasma boundary, etc. When quantified, the effect of these differences was found to be significant which was the rationale for updating/rerunning the GO cases. We assumed that the plasma is surrounded by an infinitely conducting wall at the plasma boundary itself and  $T = 1$  eV (fixed) as the temperature boundary condition. Parameterization of the Spitzer electrical resistivity  $\eta$  with respect to effective ion charge  $Z_{\text{eff}}$  is given by

$$\eta = \eta_{\text{sp},c} \times Z_{\text{eff}} \times \left( \frac{1 + 1.198Z_{\text{eff}} + 0.222Z_{\text{eff}}^2}{1 + 2.966Z_{\text{eff}} + 0.753Z_{\text{eff}}^2} \right),$$

where  $\eta_{\text{sp},c} \propto T_e^{-3/2}$  is the classical Spitzer resistivity in the absence of impurities (Hirshman, 1978).

For the purpose of this benchmark, in JOREK, we set the electric potential and the parallel ion-velocity to zero everywhere in the domain, i.e.,  $u = 0$  and  $v_{\parallel} = 0$ , along with  $\tau_{\text{IC}} = 0$ . Hence, there are no ion-flows involved as it is in the GO code. Furthermore, we use a constant viscosity  $\mu = 5.16 \times 10^{-6} \text{ kg m}^{-1} \text{ s}^{-1}$ , particle diffusivities  $D_{\parallel,D} = D_{\parallel,\text{imp}} = D_{\perp,D} = D_{\perp,\text{imp}} = D_{\text{DN}} = 0.015 \text{ m}^2 \text{ s}^{-1}$ ,  $D_{\parallel,\text{RE}} = 1.54 \text{ m}^2 \text{ s}^{-1}$ ,  $k_{\parallel} = 1.5 \times 10^{26} \text{ m}^{-1} \text{ s}^{-1}$ , particle sources  $S_D = S_{\text{imp}} = 0$ , and the RE advection factor  $f = 10^{-3}$ . It must be noted that precise values of parallel transport coefficients are irrelevant for this particular benchmark (as long as they are sufficiently large to ensure minimal gradients in the poloidal direction), since we are interested only in minor-radial dynamics. All the GO runs are terminated at the instant when the RE current begins to drop.

#### B. Results and comparison

The results obtained with GO and JOREK are compared in this section. The comparison is made with respect to the time evolution of total plasma current and RE current, and the profiles of electron temperature and RE current density. Though JOREK was run using a high-aspect ratio ( $R = 50$  m) to mimic the 1D nature of GO, there is a weak variation of physical quantities within flux-surfaces. Therefore, we use flux-surface averaged quantities from JOREK for the comparison (also the minor-radius is flux-surface averaged).

Figure 1 shows the evolution of total plasma current and the RE current for both the cases. The effect of partially ionized impurities is highlighted here, with much larger RE current beam in the case of pure Neon injection (case A). A good match is observed between GO and JOREK in both cases. The corresponding final RE current-density profiles are shown in Fig. 1, along with the common initial current-density profile. The peaked profiles typical of RE beams also show a decent match between both the codes for the cases considered.

**TABLE I.** Cases considered for the benchmark of JOREK with the 1D code GO.

Run	$n_D/n_{e0}$	$n_{\text{Ne}}/n_{e0}$	Comments
A	0	1	Pure Ne injection
B	7	0.08	D-dominated D + Ne injection

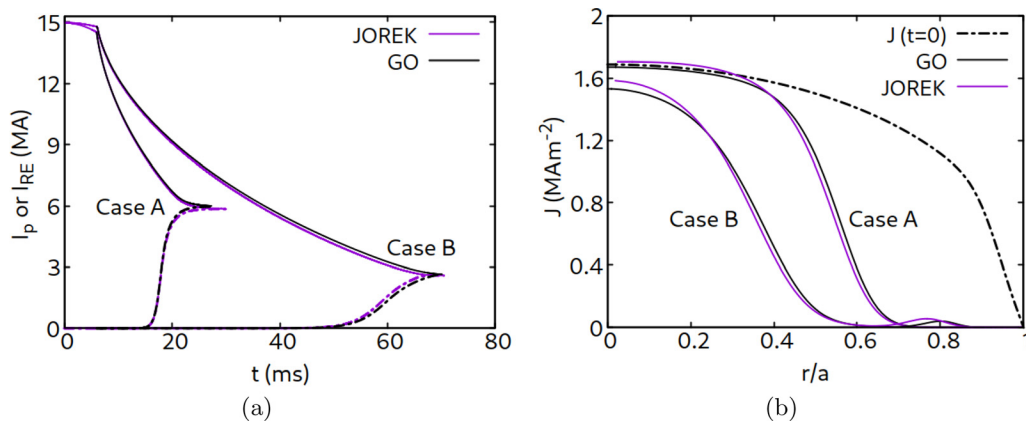


**FIG. 1.** (a) Evolution of total plasma current (full lines) and RE current (dashed lines). Simulations are stopped in the early RE plateau phase. (b) Final RE current density profiles, the black dashed line is the common initial current density profile.

The spatial profiles of electron temperature  $T_e$  are shown in Fig. 2. As can be seen, the plasma eventually cools to very low temperatures  $\sim 1$  eV in all cases. When the thermal evolution is switched-on, the temperature first drops and settles at temperatures  $\sim 6 - 9$  eV, which happens long before any significant RE current is formed. For case A, there is little thermal variation after this until RE conversion takes place. Formation of RE current reduces Ohmic heating which, in turn, triggers further cooling of the plasma to temperatures  $\sim 1$  eV. This sequence of events is seen clearly for case A in Fig. 2.

For Deuterium dominated injections, an additional effect of temperature flattening from the plasma boundary is very pronounced. This occurs because of significant neutrals near the boundary, which increases Deuterium line-radiation, which in turn cools the plasma further and forms more neutrals and so on. The “front” describing the transition from D-ions to D-neutrals is very sharp and moves toward the core, causing sequential flattening of  $T_e$  starting from the boundary. A good match is observed in general for the cases considered. However, the temperature profile at the later time for case B only matches qualitatively. This is mainly a time-shift, and the reason for this is not fully clear. A more comprehensive comparison of the

evolution of temperature and RE current density profiles is shown via the color maps in Figs. 3 and 4, respectively, for case A and case B. Note that the imposed artificial cooling phase over the first  $\approx 6$  ms is omitted in these figures. An excellent agreement is seen for both the cases.

#### IV. BENCHMARK WITH THE 2D CODE DINA

##### A. Overview of the simulation setup

DINA is a two-dimensional (axisymmetric) free-boundary equilibrium solver that includes a runaway electron fluid model and also a module to track impurities (Khayrutdinov and Lukash, 1993; Khayrutdinov *et al.*, 2001). Among others, DINA has been extensively used to characterize mitigated and unmitigated major disruptions and VDEs in ITER. As mentioned earlier, this benchmark is related to the simultaneous RE beam formation and a cold VDE in an ITER relevant scenario. For the setup used for this benchmark, an elongated ITER plasma (without any impurities) is considered that is in free-boundary equilibrium, with a toroidal plasma current  $I_p = 15$  MA, a uniform electron density of  $n_e = 10^{19} \text{ m}^{-3}$ , a core electron temperature  $T_{e,\text{core}} \approx 15 \text{ keV}$ , a central safety factor  $q_0 \approx 1$ , and an edge safety

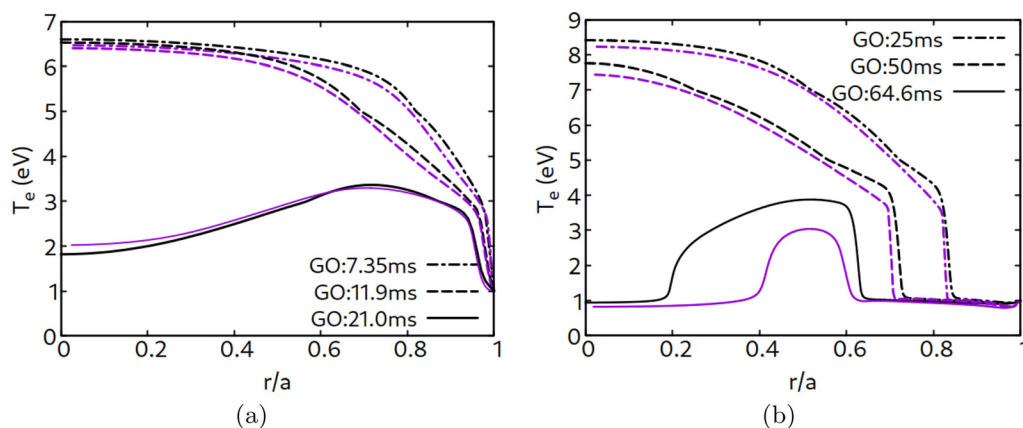


**FIG. 2.** Electron temperature profiles at different time instances for (a) case A and (b) case B.



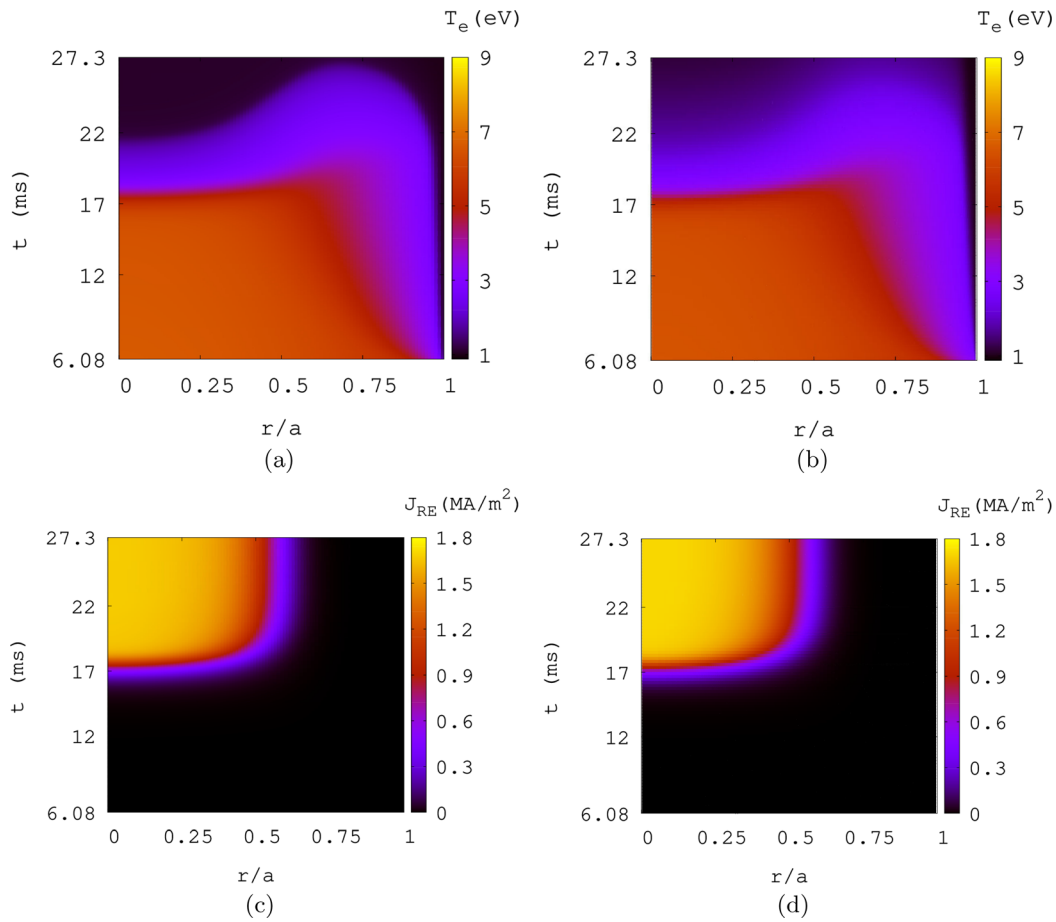


**FIG. 3.** Spatiotemporal evolution of electron temperature and RE current density for case A (pure Neon injection), starting from a time point slightly after the end of artificial cooling: (a)  $T_e$ :GO, (b)  $T_e$ :JOREK, (c)  $J_{RE}$ :GO, and (d)  $J_{RE}$ :JOREK.

factor  $q_{\text{edge}} \approx 3.7$ . The conducting structures (around the plasma) considered correspond to those of the actual configuration of ITER. They include the vacuum vessel (both the inner and outer shells), the poloidal field (PF) coils (PF1–PF6), the central solenoid (CS1–CS6), the outer triangular support (OTS), and the divertor inboard rail (DIR). Among these the vacuum vessel, OTS and DIR are passive structures, the most important in the present context of an ITER VDE being the vacuum vessel with an electrical resistivity  $\eta_{\text{wall}} = 0.8 \times 10^{-6} \Omega\text{m}$  and a thickness of 6 cm for each shell. The starting equilibrium plasma profiles and magnetic flux contours are shown in Fig. 5, and the configuration of the conducting structures is shown in Fig. 6. Coupling of the plasma with external conductors as well as vacuum is incorporated via integral electromagnetic boundary conditions (using Greens functions), usually referred to as the JOREK–STARWALL coupling (Merkel and Sempf 2006; Hoelzl *et al.*, 2012; Artola, 2018; and Artola *et al.*, 2022).

For the initial 1.5 ms in the simulation, the system is evolved so as to largely resemble the initial plasma equilibrium state but allowing the existence of  $\mathbf{E} \times \mathbf{B}$  flows in the plasma. Subsequently, for over a time of 0.5 ms (from  $t = 1.5$  to  $t = 2$  ms), the plasma is artificially cooled so as to attain an on-axis electron temperature  $T_{e,\text{core}} \approx 20$  eV by the

end of this phase. The artificial cooling is executed via a large perpendicular thermal diffusivity  $k_{\perp} = 1.27 \times 10^{24} \text{ m}^{-1} \text{ s}^{-1}$  during that time period. The temperature profiles at  $t = 2$  ms (after the artificial cooling) can be seen in Fig. 7. At  $t = 2$  ms, the artificial cooling is switched off, and pure Neon as well as an artificial RE seed population is introduced within the last closed flux surface (LCFS) of the plasma domain with a spatially uniform-density. A total of  $\approx 4.88 \times 10^{22}$  Neon particles, corresponding to a Neon number density  $n_{\text{imp}} = 0.62 \times 10^{20} \text{ m}^{-3}$  are introduced. The introduction of Neon is intended to mimic an idealized massive material injection in the context of a disruption mitigation system in ITER. Likewise, the artificial RE seed intends to loosely represent the seed of REs that would have been generated during the thermal quench via the mechanisms of hot-tail, Compton scattering, Tritium decay, and Dreicer. It must be noted that the introduction of the artificial RE seed is done only once (at the end of TQ), and there is no continued seed generation during the current quench (tritium and compton seeds are switched-off throughout the simulation). After the injection, due to impurity radiation, the plasma tends to further cooldown to lower temperatures. At the same time, due to the increased plasma resistivity at low-temperatures, the plasma current decays (current quench), along with the conversion of thermal

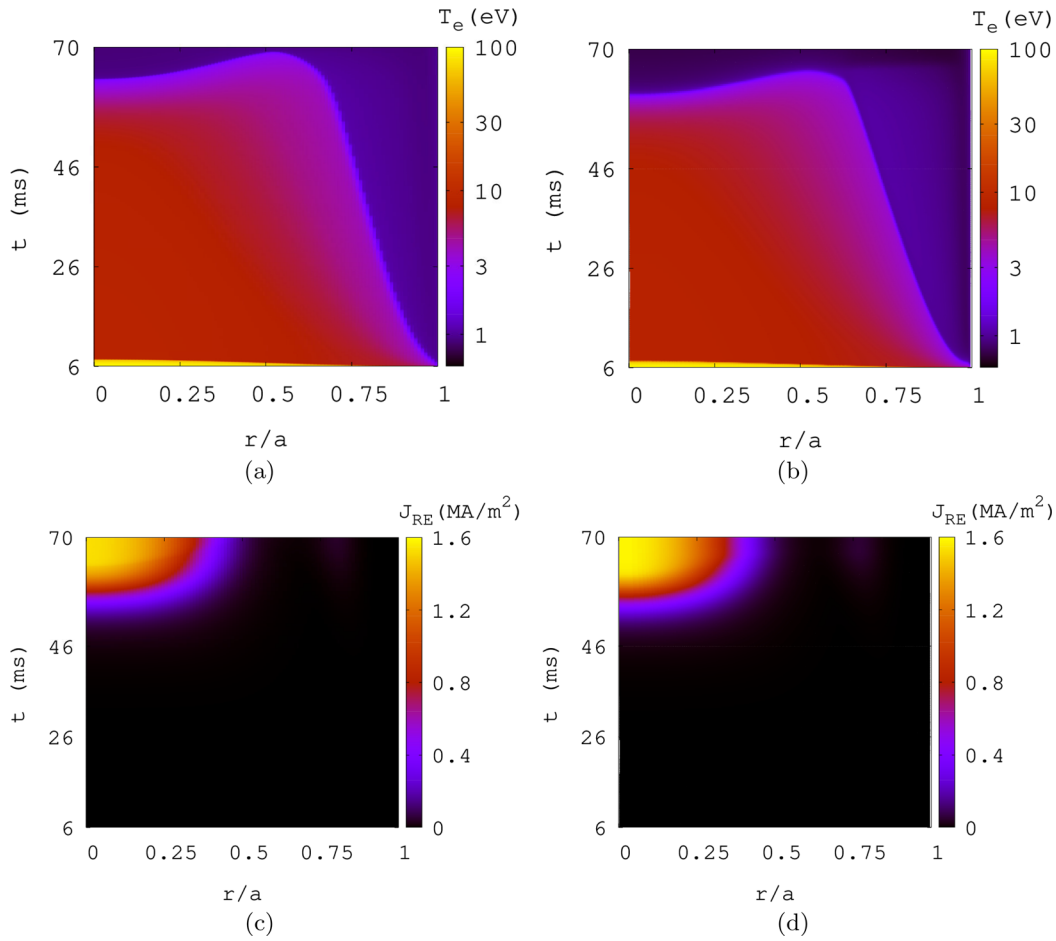


**FIG. 4.** Spatiotemporal evolution of electron temperature and RE current density for case B, starting from the time point immediately after the end of artificial cooling: (a)  $T_e$ : GO, (b)  $T_e$ :JOREK, (c)  $J_{RE}$ :GO, and (d)  $J_{RE}$ :JOREK.

current to RE current via the avalanche mechanism. During and after the current quench, the plasma becomes vertically unstable and moves upward, representing what is typically referred to as a cold VDE. Such an upward motion leads to a continuous shrinking of the plasma due to scraping-off with the wall and the eventual loss of the whole plasma column. The aim of this study is to see how the results of a similar but not identical simulation and model setup in JOREK compares to the DINA results. Likewise, the aim of this specific study has not been to replicate all details of the DINA simulation precisely, but rather to mimic the important features of the DINA simulation.

There exist some important differences in the plasma modeling in JOREK and DINA, which are discussed hereby. First, DINA evolves/tracks individual ion charge-states of the impurity species, while JOREK (in the version used in this study) uses a coronal-equilibrium model for the same. However, for reference, we also use the data of a DINA simulation that was performed in a way that mimics (to some extent) a coronal-equilibrium behavior. In addition, in the DINA simulation, a large radial diffusion coefficient is applied to the density of each impurity charge-state (the diffusion coefficient is large enough to keep the density profiles nearly flat and so the precise

value does not matter). This is done in order to ensure that the impurities that are introduced on the boundary diffuse into the plasma core without remaining near the edge. However, this makes the charge-state densities and hence the effective ion-charge ( $Z_{eff}$ ) radially uniform even when there is a large temperature variation radially. While this might appear rather unphysical, in the present simulation scenario, after about  $t \approx 10$  ms, the temperature profile becomes rather flat. So such a treatment in DINA (of using a large radial charge-state diffusion) is not expected to affect the results much beyond a simulation time  $t \approx 10$  ms, which is the zone of primary interest for the comparison. Finally, unlike JOREK, DINA neglects the effect of partially-ionized impurities in computing the RE avalanche source, a point that we will revisit shortly when analyzing the results.

In the present benchmark study, the Deuterium neutral density is set to zero ( $\rho_n = 0$ ) and is not evolved. This is done in order to correspond to the DINA simulations. In addition, for the temperatures encountered in this specific simulation, the neutral population is expected to be negligible and hence the assumption is expected to have an insignificant effect. For the particle diffusivities, we used  $D_{||,D} = D_{||,imp} = 1.54 \text{ m}^2 \text{ s}^{-1}$  and  $D_{\perp,D} = D_{\perp,imp} = 6.2 \text{ m}^2 \text{ s}^{-1}$ . The background

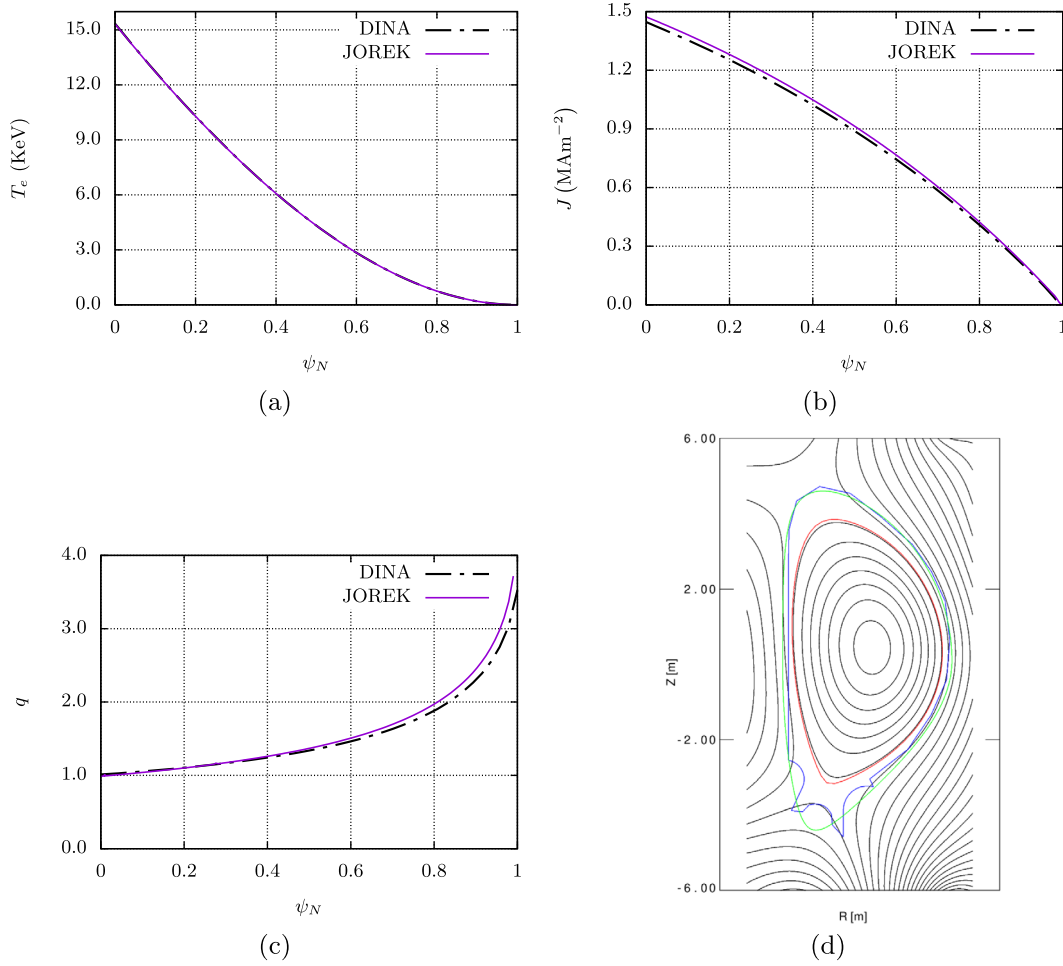


**FIG. 5.** Initial equilibrium plasma profiles of (a) electron temperature, (b) toroidal current density, and (c) safety factor, as a function of normalized poloidal magnetic flux  $\psi_N$ ; (d) equilibrium magnetic flux contours, red: last closed flux-surface, blue: first wall, and green: simulation domain used in JOREK.

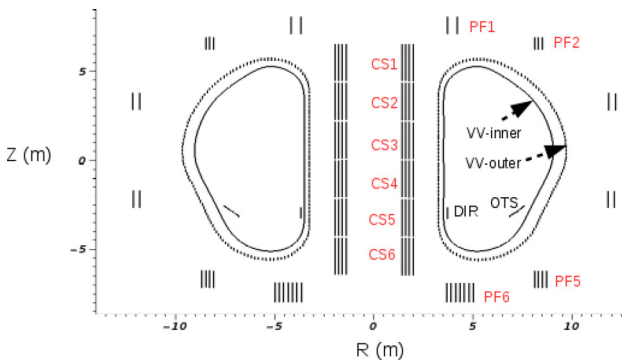


**FIG. 6.** Schematic of the active and passive conducting structures of ITER used in the simulations. Abbreviations are CS: central solenoid, PF: poloidal field coil, VV: vacuum vessel, DIR: divertor inboard rail, and OTS: outer triangular support.

plasma-fluid viscosity ( $\mu = 0.52 \times 10^{-6} \text{ kg m}^{-1} \text{ s}^{-1}$ ) and thermal diffusivity ( $k_{\perp} = 0.4 \times 10^{20} \text{ m}^{-1} \text{ s}^{-1}$ ,  $k_{\parallel} = 1.5 \times 10^{26} \text{ m}^{-1} \text{ s}^{-1}$ ) are chosen to be temperature independent, and there are no volumetric sources used for the plasma-fluid particle density and thermal energy. However, the plasma electrical resistivity ( $\eta$ ) is a function of temperature and  $Z_{\text{eff}}$  and is given by  $\eta_{\text{sp}} = \eta_{\text{sp,c}} \times Z_{\text{eff}}$ , where  $\eta_{\text{sp,c}}$  is the classical Spitzer resistivity in the absence of impurities. RE parallel transport is modeled via a large parallel diffusivity (to mimic the fast parallel advection) and so the RE advection factor  $f = 0$ . A value of  $D_{\text{RE},\parallel} = 1.54 \times 10^8 \text{ m}^2 \text{ s}^{-1}$  has been used for the JOREK results presented in this work. The choice for this value is justified through a sensitivity study that will be discussed later. For the purpose of this benchmark, in JOREK we set the parallel ion-velocity to zero everywhere in the domain, i.e.,  $v_{\parallel} = 0$ , along with  $\tau_{\text{IC}} = 0$ . Hence, there are no field-parallel and diamagnetic-drift ion-flows involved. This reduces the numerical complexity of the simulations. Furthermore, the artificial cooling (from  $t = 1.5$  to  $t = 2$  ms) is achieved

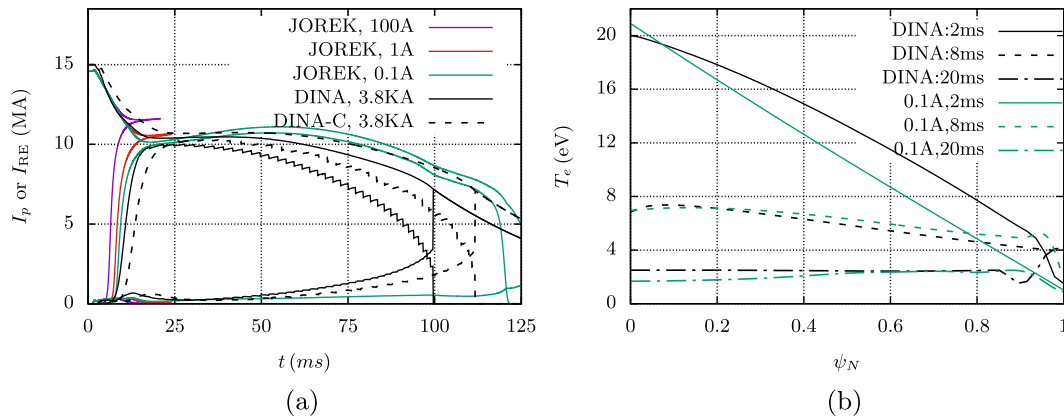


**FIG. 7.** (a) Evolution of total plasma current  $I_p$ , RE current  $I_{RE}$ , and the toroidal Halo current  $I_{halo}$  (same linetypes have been used for the three currents for easy legend readability). Values of current given in the legend represent the RE seed current used. “DINA-C” denotes a DINA simulation run in a manner so as to mimic a coronal-equilibrium like behavior; (b) electron temperature profiles at different time points in the simulation.

by the use of a large perpendicular thermal diffusivity. In the simulation considered here, the toroidal Halo currents are negligible until the plasma moves significantly upward and starts to scrape-off at the boundary. In JOREK, Halo currents are suppressed during this phase of the simulation ( $t = 1.5$  to  $t = 2$  ms) by simultaneously increasing the parallel thermal diffusivity, such that there is no accumulation of thermal energy lost by the plasma core in the scrape-off layer (SOL) and the resistivity consequently remains high there.

## B. Results and discussion

The results obtained with DINA and JOREK are compared in this section. While JOREK was run with different RE seed currents ranging from  $10^{-4}$  A to 100 A, however, for the sake of easy readability, only three selected results with different RE seed currents (0.1, 1, and 100 A) are shown in the figures. DINA results were obtained using a single much higher RE seed current value of 3.8 kA. Figure 7 shows the time evolution of the total current, RE current, and the toroidal Halo current. The plateau RE current  $\approx 10$  MA matches best between JOREK and DINA, with RE seeds of 0.1 and 1 A in JOREK, which is several orders of magnitude smaller than the RE seed of 3.8 kA used in DINA. Hence, the JOREK case with a seed current of 0.1 A has been carried out until the full RE beam termination, for

further comparison. Such a large difference in the RE seed required to obtain the same final RE beam current can be largely attributed to the neglect of the effect of partially-ionized impurities on RE avalanche in DINA. DINA results with both impurity charge state tracking and coronal equilibrium lead to roughly a similar plateau RE beam current  $\approx 10$  MA. However, with coronal equilibrium, the current decay rate is slower as expected, along with a corresponding delay in RE avalanche growth. Furthermore, the plateau RE current in JOREK is observed to have a weak dependence on the RE seed (as expected), in the range of seeds considered. An RE seed current as small as  $10^{-4}$  A still produces a plateau RE current of  $\approx 9.5$  MA (not shown in figure). This emphasizes the fact that strategies that lead only to a moderate RE seed reduction are largely ineffective (for risk mitigation) in strong-avalanche-gain machines like ITER. The increase in current during the plateau phase in JOREK is caused by the corresponding decay of vacuum-vessel toroidal current (not shown in the figure) that provides extra electric field enhancing the avalanche. The Halo current can be seen to be negligible in all cases.

Figure 7 shows the electron temperature profile at different time-instants corresponding to end-of-artificial-cooling (2 ms), before RE avalanche (8 ms), and end of RE avalanche (20 ms). Upon the introduction of Ne impurities at  $t = 2$  ms, the plasma further cools down significantly due to impurity radiation dominating over the opposing

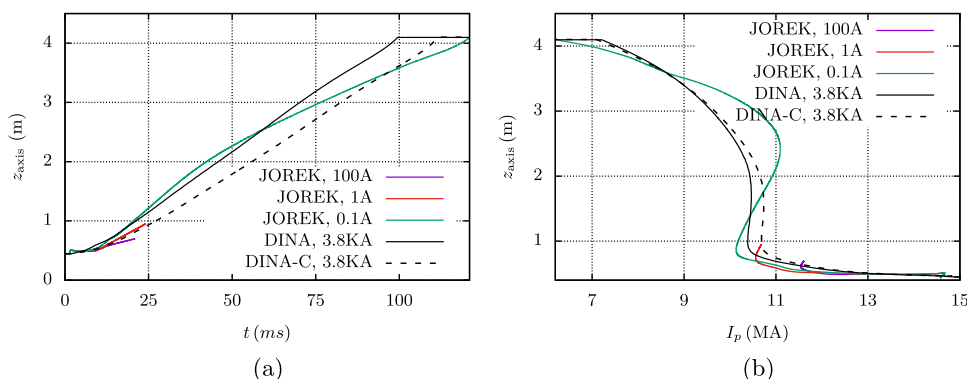


**FIG. 8.** Vertical position of the plasma magnetic axis as a function of (a) time and (b) total plasma current. Values of current given in the legend represent the RE seed current used. DINA-C implies a DINA simulation run in a manner so as to mimic a coronal-equilibrium like behavior.

effect of Ohmic heating. Reduction in Ohmic heating during RE beam formation causes the temperature to further drop to  $\sim 2$  eV with a nearly uniform minor-radial profile. A reasonable agreement between both the codes is observed. The temperature predictions from the coronal equilibrium version of the DINA simulation shows numerical oscillations (in time) between  $t \approx 3$  and  $t \approx 8$  ms. Hence, the corresponding temperature profiles are not plotted to avoid misinterpretation.

Being a vertically elongated plasma, from the start of the current quench, one can expect vertical motion of the plasma column toward the wall (cold VDE). The time evolution of the plasma vertical position is shown in Fig. 8. It can be observed that the vertical motion continues into the RE plateau phase until the final termination. The timescale of vertical motion is  $\sim 2 \times 10^{-2}$  s and is dependent on the final plateau RE current. The farther away the plateau RE current is from the initial equilibrium plasma current (of  $\approx 15$  MA), the faster is the vertical instability. Both the codes show a good match in this respect as well. It must be noted that since RE beam formation stalls the current decay, in the absence of RE beam formation (not shown here), one can expect the vertical plasma motion to be faster due to the faster current decay rate (Bandaru *et al.*, 2019).

The relevant timescales in tokamak VDEs are the poloidal Alfvén timescale  $\tau_{A,\text{pol}}$  and the vacuum-vessel  $L/R$  timescale  $\tau_{L/R}$ . In this simulation,  $\tau_{A,\text{pol}} \sim 1.1 \times 10^{-5}$  s and  $\tau_{L/R} = 0.5$  s. Since ITER's vacuum vessel is known to be strongly stabilizing, it is only the  $L/R$  timescale that is relevant in our case. The VDE growth rate in a multi-conductor system can be represented as

$$\gamma = \frac{1}{\tau_{L/R}} \left( \frac{1}{f-1} \right), \quad (f > 1),$$

where  $f$  is the stabilization parameter (that depends on mutual inductances and currents in the system) as described in Leuer (1989). The much faster timescale of the vertical motion as compared to the  $L/R$  timescale in this simulation can be attributed to a smaller value of the stabilization parameter  $f$  which decreases with the decrease in  $I_p$  (though  $I_p$  is not the only parameter that determines  $f$ ). The small Halo currents decaying quickly again could also

affect the dynamics to some extent. Evolution of the internal inductance  $li3$  is shown in Fig. 9 and one can see that over time there is a significant difference between DINA and JOREK. This can be attributed to several reasons. For example, a noticeable difference between the current profiles is observed already when the full RE beam forms due to the different RE source models in both codes. Furthermore, it is possible that the exact definition (especially the domain of integration used) for computing the internal inductance might be different in both the codes.

Figure 8 shows the dependence of the vertical position on the total plasma current. It can be observed that the vertical motion occurs even at a nearly constant  $I_p$ . Of particular interest in this case is the effect of vacuum-vessel resistivity on the speed of the vertical motion. Figure 9 shows the sensitivity of the VDE timescale to the vacuum-vessel resistivity. The parameter  $\eta_{w,\text{fact}}$  represents the factor by which the vessel resistivity is multiplied in each case. It can be seen that with the actual resistivity of the ITER vacuum vessel ( $\eta_{w,\text{fact}} = 1$ ), we do not see a convergent behavior in terms of the vacuum-vessel acting like an ideal wall. A further decrease by a factor  $\sim 10$  or more leads to a disappearance of the fast vertical motion. The halo currents, in fact, drop to negligible values in the lower vessel resistivity cases.

## V. SUMMARY AND OUTLOOK

RE mitigation experiments with massive material injection often show that the plasma cools down to temperatures where partial-ionization and neutralization effects become rather important. Within this context, recent model extensions in JOREK related to the RE fluid model considering the effects of partially ionized impurities and deuterium neutrals have been presented. Such an RE fluid model coupled with background plasma MHD can potentially offer significant insights into the physics of RE beam formation and mitigation, without being prohibitively expensive. Several studies of RE beam dynamics, both in relation to the existing tokamak experiments as well as ITER are already under way using the model presented here. Those studies are outside of scope of the present paper and will be reported elsewhere. Several possibilities exist to further improve the model. Including the effects of enhanced scattering by REs, non-coronal equilibrium models for impurities, modified plasma equilibrium in the

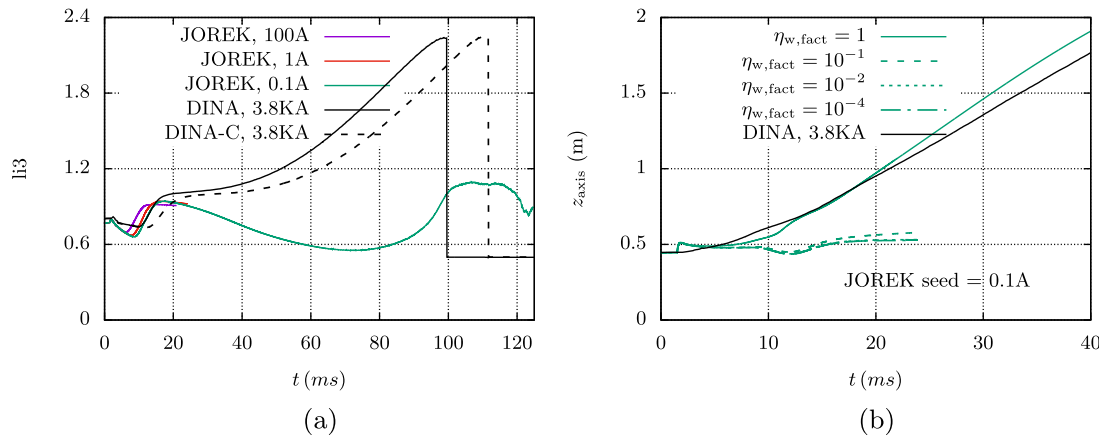


**FIG. 9.** (a) Internal inductance as a function of time, (b) effect of wall resistivity on the plasma vertical motion. The variable  $\eta_{w,\text{fact}}$  refers to the factor by which the actual ITER vacuum vessel resistivity is multiplied.



presence of high-energy REs, two/three-temperature models would be some of the avenues in this regard. Furthermore, JOREK was separately benchmarked with the GO and DINA codes, covering aspects ranging from thermal and RE current density evolution to the dynamics of a cold VDE. A good agreement has been observed with both the codes. In view of the importance of the RE problem to ITER, the authors would welcome further benchmarks (especially for 3D scenarios) with other large fusion plasma MHD codes. It must be noted that material injections in the present work were not localized as would be the case with the SPI strategy in ITER. Models for SPI already exist in JOREK and have been used for modeling disruptions in JET (Hu *et al.*, 2018) and ITER (Hu *et al.*, 2023) with SPI. Therefore, applying the RE fluid model in JOREK in combination with SPI for 3D simulations is, in principle, possible. However, the effect of REs on the ablation of the shattered pellets has yet to be included to make the model more realistic. Efforts in that direction are currently ongoing.

## ACKNOWLEDGMENTS

The authors acknowledge fruitful discussions with E. Nardon (CEA). We also acknowledge help from V. E. Lukash for sharing DINA simulation data for the benchmark. This work has been carried out within the framework of the ITER implementing agreement No. 3, Ref: IO/IA/20/4300002200. ITER is the Nuclear Facility INB No. 174. This work explores the physics processes during plasma operation of the tokamak when disruptions take place; nevertheless, the nuclear operator is not constrained by the results presented here. The views and opinions expressed herein do not necessarily reflect those of the ITER Organization. Part of this work was supported by the EUROfusion—Theory and Advanced Simulation Coordination (E-TASC) via the theory and simulation verification and validation (TSVV) project on MHD transients (2021-2025). Part of this work has been carried out within the framework of the EUROfusion Consortium, funded by the European Union via the Euratom Research and Training Programme (Grant Agreement No. 101052200 of EUROfusion). Views and opinions expressed are, however, those of the author(s) only and do not necessarily reflect those of the European Union or the European Commission. Neither the European Union nor the European Commission can be held responsible for them.

## AUTHOR DECLARATIONS

### Conflict of Interest

The authors have no conflicts to disclose.

### Author Contributions

**V. Bandaru:** Conceptualization (lead); Data curation (lead); Formal analysis (lead); Funding acquisition (equal); Investigation (equal); Methodology (equal); Project administration (equal); Resources (equal); Software (lead); Validation (equal); Visualization (equal); Writing – original draft (lead); Writing – review & editing (equal). **M. Hoelzl:** Conceptualization (equal); Funding acquisition (lead); Investigation (equal); Methodology (equal); Project administration (equal); Resources (equal); Software (supporting); Supervision (lead); Validation (supporting); Writing – original draft (supporting); Writing – review & editing (equal). **F. J. Artola:** Conceptualization

(supporting); Investigation (supporting); Validation (equal); Writing – review & editing (supporting). **O. Vallhagen:** Validation (equal); Writing – review & editing (supporting). **M. Lehnen:** Conceptualization (supporting); Funding acquisition (supporting); Investigation (supporting); Methodology (supporting); Project administration (supporting); Resources (supporting); Supervision (supporting). **The JOREK Team:** Funding acquisition (equal); Software (equal); Validation (equal).

## DATA AVAILABILITY

The data that support the findings of this study are available from the corresponding author upon reasonable request.

## REFERENCES

- Artola, F. J., “Free-boundary simulations of MHD plasma instabilities in tokamaks,” Ph.D. thesis (Université Aix Marseille, 2018).
- Artola, F. J., Loarte, A., Hoelzl, M., Lehnen, M., Schwarz, N., and the JOREK Team, “Non-axisymmetric MHD simulations of the current quench phase of ITER mitigated disruptions,” *Nucl. Fusion* **62**(5), 056023 (2022).
- Bandaru, V., Hoelzl, M., Artola, F. J., Papp, G., and Huijsmans, G. T. A., “Simulating the nonlinear interaction of relativistic electrons and tokamak plasma instabilities: Implementation and validation of a fluid model,” *Phys. Rev. E* **99**, 063317 (2019).
- Bandaru, V., Hoelzl, M., Reux, C., Ficker, O., Silburn, S., Lehnen, M., Eidietis, N., Contributors, J.E.T., and JOREK Team, “Magnetohydrodynamic simulations of runaway electron beam termination in JET,” *Plasma Phys. Controlled Fusion* **63**, 035024 (2021).
- Breizman, B. N., Aleynikov, P., Hollmann, E. M., and Lehnen, M., “Physics of runaway electrons in tokamaks,” *Nucl. Fusion* **59**(8), 083001 (2019).
- Czarny, O. and Huysmans, G. T. A., “Bezier surfaces and finite elements for MHD simulations,” *J. Comput. Phys.* **227**(16), 7423–7445 (2008).
- Fülöp, T., Helander, P., Vallhagen, O., and Embréus, O., others, “Effect of plasma elongation on current dynamics during tokamak disruptions,” *J. Plasma Phys.* **86**(1), 474860101 (2020).
- Hender, T. C., Wesley, J. C., Bialek, J., Bondeson, A., Boozer, A. H., Buttery, R. J., Garofalo, A., Goodman, T. P., Granetz, R. S., Gribov, Y., and Gruber, O., “Disruption and magnetic control topical group 2007 Chapter 3: MHD stability, operational limits and disruptions,” *Nucl. Fusion* **47**(6), S128 (2007).
- Hesslow, L., Embréus, O., Stahl, A., DuBois, T. C., Papp, G., Newton, S. L., and Fülöp, T., “Effect of partially screened nuclei on fast-electron dynamics,” *Phys. Rev. Lett.* **118**, 255001 (2017).
- Hesslow, L., Embréus, O., Vallhagen, O., and Fülöp, T., “Influence of massive material injection on avalanche runaway generation during tokamak disruptions,” *Nucl. Fusion* **59**(8), 084004 (2019).
- Hesslow, L., Embréus, O., Wilkie, G. J., Papp, G., and Fülöp, T., “Effect of partially ionized impurities and radiation on the effective critical electric field for runaway generation,” *Plasma Phys. Controlled Fusion* **60**, 074010 (2018).
- Hirshman, S. P., “Neoclassical current in a toroidally-confined multispecies plasma,” *Phys. Fluids* **21**(8), 1295–1301 (1978).
- Hoelzl, M., Huijsmans, G. T. A., Pamela, S. J. P., Becoulet, M., Nardon, E., Artola, F. J., Nkong, B., Atanasiu, C. V., Bandaru, V., Bhole, A., and Bonfiglio, D., “The JOREK non-linear extended MHD code and applications to large-scale instabilities and their control in magnetically confined fusion plasmas,” *Nucl. Fusion* **61**(6), 065001 (2021).
- Hoelzl, M., Merkel, P., Huysmans, G. T. A., Nardon, E., Strumberger, E., McAdams, R., Chapman, I., Günter, S., and Lackner, K., “Coupling JOREK and STARWALL codes for non-linear resistive-wall simulations,” *J. Phys.: Conf. Ser.* **401**(1), 012010 (2012).
- Hu, D., Huijsmans, G. T. A., Nardon, E., Hoelzl, M., Lehnen, M., Bonfiglio, D., and JOREK team, “Collisional-radiative non-equilibrium impurity treatment for JOREK simulations,” *Plasma Phys. Controlled Fusion* **63**(12), 125003 (2021).
- Hu, D., Nardon, E., Artola, F. J., Lehnen, M., Bonfiglio, D., Hoelzl, M., Huijsmans, G. T. A., Lee, S. J., and Jorek Team, “Collisional-radiative

- simulation of impurity assimilation, radiative collapse and MHD dynamics after ITER shattered pellet injection," *Nucl. Fusion* **63**(6), 066008 (2023).
- Hu, D., Nardon, E., Lehnen, M., Huijsmans, G. T. A., van Vugt, D. C., and Contributors, JET, "3D non-linear MHD simulation of the MHD response and density increase as a result of shattered pellet injection," *Nucl. Fusion* **58**(12), 126025 (2018).
- Khayrutdinov, R. R. and Lukash, V. E., "Studies of plasma equilibrium and transport in a tokamak fusion device with the inverse-variable technique," *J. Comput. Phys.* **109**(2), 193–201 (1993).
- Khayrutdinov, R. R., Lister, J. B., Lukash, V. E., and Wainwright, J. P., "Comparing DINA code simulations with TCV experimental plasma equilibrium responses," *Plasma Phys. Controlled Fusion* **43**(3), 321 (2001).
- Korving, S. Q., Mitterauer, V., Huijsmans, G. T. A., Loarte, A., Hoelzl, M., JOREK team, and ASDEX Upgrade team, "Simulation of neoclassical heavy impurity transport in ASDEX Upgrade with applied 3D magnetic fields using the nonlinear MHD code JOREK," *Phys. Plasmas* **31**, 052504 (2024).
- Korving, S. Q., Huijsmans, G. T. A., Park, J.-S., Loarte, A., and Jorek Team, "Development of the neutral model in the nonlinear MHD code JOREK: Application to  $E \times B$  drifts in ITER PFPO-1 plasmas," *Phys. Plasmas* **30**(4), 042509 (2023).
- Leuer, J. A., "Passive vertical stability in the next generation tokamaks," *Fusion Technol.* **15**(2P2A), 489–494 (1989).
- Liu, C., Zhao, C., Jardin, S. C., Ferraro, N. M., Paz-Soldan, C., Liu, Y., and Lyons, B. C., "Self-consistent simulation of resistive kink instabilities with runaway electrons," *Plasma Phys. Controlled Fusion* **63**(12), 125031 (2021).
- Martín-Solís, J. R., Loarte, A., and Lehnen, M., "Formation and termination of runaway beams in ITER disruptions," *Nucl. Fusion* **57**(6), 066025 (2017).
- Matsuyama, A., Aiba, N., and Yagi, M., "Reduced fluid simulation of runaway electron generation in the presence of resistive kink modes," *Nucl. Fusion* **57**(6), 066038 (2017).
- Merkel, P. and Sempf, M., "Feedback stabilization of resistive wall modes in the presence of multiply connected wall structures," in *IAEA Fusion Energy Conference* (International Atomic Energy Agency, 2006), paper TH/P3-8, [https://www-pub.iaea.org/MTCD/Meetings/FEC2006/th\\_p3-8.pdf](https://www-pub.iaea.org/MTCD/Meetings/FEC2006/th_p3-8.pdf).
- Mosher, D., "Coronal equilibrium of high-atomic-number plasmas," *Phys. Rev. A* **10**, 2330–2335 (1974).
- Papp, G., Fülöp, T., Fehér, T., de Vries, P. C., Riccardo, V., Reux, C., Lehnen, M., Kiptily, V., Plyusnin, V. V., Alper, B., and JET EFDA Contributors, "The effect of ITER-like wall on runaway electron generation in JET," *Nucl. Fusion* **53**(12), 123017 (2013).
- Sainterme, A. P. and Sovinec, C. R., "Resistive hose modes in tokamak runaway electron beams," *Phys. Plasmas* **31**(1), 010701 (2024).
- Vallhagen, O., Embreus, O., Pusztai, I., Hesslow, L., and Fülöp, T., "Runaway dynamics in the DT phase of ITER operations in the presence of massive material injection," *J. Plasma Phys.* **86**(4), 475860401 (2020).